



UNIVERSITY OF LEEDS

This is a repository copy of *Stereo Imaging Camera Model for 3D Shape Reconstruction of Complex Crystals and Estimation of Facet Growth Kinetics*.

White Rose Research Online URL for this paper:
<http://eprints.whiterose.ac.uk/107823/>

Version: Accepted Version

Article:

Zhang, R, Ma, CY, Liu, JJ et al. (3 more authors) (2017) Stereo Imaging Camera Model for 3D Shape Reconstruction of Complex Crystals and Estimation of Facet Growth Kinetics. *Chemical Engineering Science*, 160. pp. 171-182. ISSN 0009-2509

<https://doi.org/10.1016/j.ces.2016.11.029>

© 2016 Published by Elsevier Ltd. Licensed under the Creative Commons Attribution-NonCommercial-NoDerivatives 4.0 International
<http://creativecommons.org/licenses/by-nc-nd/4.0/>

Reuse

Unless indicated otherwise, fulltext items are protected by copyright with all rights reserved. The copyright exception in section 29 of the Copyright, Designs and Patents Act 1988 allows the making of a single copy solely for the purpose of non-commercial research or private study within the limits of fair dealing. The publisher or other rights-holder may allow further reproduction and re-use of this version - refer to the White Rose Research Online record for this item. Where records identify the publisher as the copyright holder, users can verify any specific terms of use on the publisher's website.

Takedown

If you consider content in White Rose Research Online to be in breach of UK law, please notify us by emailing eprints@whiterose.ac.uk including the URL of the record and the reason for the withdrawal request.

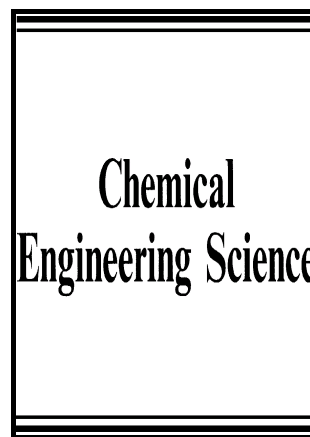


eprints@whiterose.ac.uk
<https://eprints.whiterose.ac.uk/>

Author's Accepted Manuscript

Stereo Imaging Camera Model for 3D Shape Reconstruction of Complex Crystals and Estimation of Facet Growth Kinetics

Rui Zhang, Cai Y. Ma, Jing J. Liu, Yang Zhang, Yu J. Liu, Xue Z. Wang



www.elsevier.com/locate/ces

PII: S0009-2509(16)30624-8
DOI: <http://dx.doi.org/10.1016/j.ces.2016.11.029>
Reference: CES13252

To appear in: *Chemical Engineering Science*

Received date: 3 May 2016
Revised date: 29 October 2016
Accepted date: 14 November 2016

Cite this article as: Rui Zhang, Cai Y. Ma, Jing J. Liu, Yang Zhang, Yu J. Liu and Xue Z. Wang, Stereo Imaging Camera Model for 3D Shape Reconstruction of Complex Crystals and Estimation of Facet Growth Kinetics, *Chemical Engineering Science*, <http://dx.doi.org/10.1016/j.ces.2016.11.029>

This is a PDF file of an unedited manuscript that has been accepted for publication. As a service to our customers we are providing this early version of the manuscript. The manuscript will undergo copyediting, typesetting, and a review of the resulting galley proof before it is published in its final citable form. Please note that during the production process errors may be discovered which could affect the content, and all legal disclaimers that apply to the journal pertain.

Stereo Imaging Camera Model for 3D Shape Reconstruction of Complex Crystals and Estimation of Facet Growth Kinetics

Rui Zhang^{a,b}, Cai Y. Ma^a, Jing J. Liu^a, Yang Zhang^{a*}, Yu J. Liu^c, Xue Z. Wang^{a,b,1*}

^aSchool of Chemistry and Chemical Engineering, South China University of Technology, Guangzhou, China 510640

^bSchool of Chemical and Process Engineering, University of Leeds, Leeds LS2 9JT, U.K.

^cPharmaVision (Qingdao) Ltd, 226A, Building A1, Area A1, 17 Songyuan Road, Qingdao Industrial Technology Research Institute, Qingdao Hi-Tech Development Zone, Qingdao City, Shandong Province, China 266109

ceyzhang@scut.edu.cn

xuezhongwang@scut.edu.cn

x.z.wang@leeds.ac.uk

***Corresponding author.** Professor Xue Z. Wang China One Thousand Talent Scheme Professor School of Chemistry and Chemical Engineering South China University of Technology 381 Wushan Rd, Tianhe District Guangzhou, PR China 510641 Tel.: +86 20 8711 4000; fax: +86 20 8711 4000

***Corresponding author.** Dr Yang Zhang Lecturer School of Chemistry and Chemical Engineering South China University of Technology 381 Wushan Rd, Tianhe District Guangzhou, PR China 510641 Tel.: +86 20 8711 4000; fax: +86 20 87114000

¹ Chair in Intelligent Measurement and Control School of Chemical and Process Engineering University of Leeds Leeds LS2 9JT, UK Tel +44 113 343 2427; fax +44 113 343 2384

Abstract

The principle that the 3D shape of crystals that grow from a solution can be characterised in real-time using stereo imaging has been demonstrated previously. It uses the 2D images of a crystal that are obtained from two or more cameras arranged in defined angles as well as a mathematical reconstruction algorithm. Here attention is given to the development of a new and more robust 3D shape reconstruction method for complicated crystal structures. The proposed stereo imaging camera model for 3D crystal shape reconstruction firstly rotates a digitised crystal in the three-dimensional space and varies the size dimensions in all face directions. At each size and orientation, 2D projections of the crystal, according to the angles between the 2D cameras, are recorded. The contour information of the 2D images is processed to calculate Fourier descriptors and radius-based signature that are stored in a database. When the stereo imaging instrument mounted on a crystalliser captures 2D images, the images are segmented to obtain the contour information and processed to obtain Fourier descriptors and radius-based information. The calculated Fourier descriptors and radius-based signature are used to find the best matching in the database. The corresponding 3D crystal shape is thus found. Potash alum crystals that each has 26 habit faces were used as a case study. The result shows that the new approach for 3D shape reconstruction is more accurate and significantly robust than previous methods. In addition, the growth rates of $\{111\}$, $\{110\}$ and $\{100\}$ faces were correlated with relative supersaturation to derive models of facet growth kinetics.

Keywords: Online stereo imaging, Camera model, Crystal shape reconstruction, Potash alum, Crystal Facet growth kinetics

Nomenclature

A	projection area
ATR FTIR	attenuated total reflectance Fourier transform infrared spectroscopy
a, b, c	unit cell parameters (length) (Å)
C	solute concentration (g/L)
C*	solubility (g/L)
f	the distance from camera centre to the image plane
F	the Fourier coefficients
FDs	the Fourier descriptors
FD _i	Fourier descriptors
FD _{1,i}	the i th Fourier descriptor of the images 1
FD _{2,i}	the i th Fourier descriptor of the images 2
H	normal distances of feature faces
k _i	the pixel point
K	number of sampled boundary pixels
j	the imaginary unit
s	solute mole fraction
SD	the similarity distance
m	the value of sin (θ)
n _j	the number of vertices in the convex hull
n	the sample point in Fourier transform
n _{x,y,z}	the number of selected size in each database
n _{δ,θ,φ}	the number of rotation angle in each database
N	matrix of face normal
P _i	vector of the projected crystal vertices
r _i	centroid to boundary distance
T	temperature (°C)
t	time (s)
v	the 3×1 vector of coordinates on a plane
V	coordinates of crystal vertex
V _{111}	growth rate of face {111} (m/s)
V _{110}	growth rate of face {110} (m/s)
V _{100}	growth rate of face {100} (m/s)
w	the number of the featured faces of a crystal
x	the mapped point on a plane
X _i , Y _i	the vertex coordinates of projection
X _c , Y _c	the centroid of projection
x, y, z	Cartesian coordinates (μm)
Greek letters	
α, β, γ	unit cell parameters (angle) (°)
δ, θ, φ	Euler angles
ε	centroid to boundary angle
σ	relative supersaturation

1. Introduction

Engineering crystal shape and crystal shape distribution (CShD) is an important direction of research in solution crystallisation (Lovette et al., 2008), and advances in measurement, modelling and closed-loop control of crystal shape and CShD were recently reviewed (Ma et al., 2016). On measurement, on-line microscopic imaging and image analysis for real-time characterisation of the shape and CShD of crystals in a crystalliser has attracted much attention in recent years (Barrett and Glennon, 2002; Calderon de Anda et al., 2005a; Calderon De Anda et al., 2005b; Huo et al., 2016; Larsen and Rawlings, 2009; Larsen et al., 2006; Patience and Rawlings, 2001; Wang et al., 2007; Zhang et al., 2015; Zhao et al., 2013; Zhou et al., 2011; Zhou et al., 2009). There are also readily available products on the market such as Mettler Toledo's PVM, MessTechnik's PIA, PharmaVision (Qingdao) Ltd's 2D Process Vision Probe. The current research is motivated by the observation that previous work has focused on 2D imaging. Since crystals in a stirred tank crystalliser undergo continuous rotation and motion, crystal size estimation using 2D imaging could lead to large errors compared to 3D imaging method. In a recent study (Zhang et al., 2015), it was found that for needle-like crystals, 2D imaging significantly underestimated the size of crystals.

Methods alternative to 2D imaging were investigated for the purpose of more accurate estimation of crystal shape and size. Li et al. (Li et al., 2006) made probably the first attempt to obtain 3D crystal shape information based on on-line obtained 2D crystal images taken from a crystalliser, and the method was named a camera model. The camera model rotates a digital 3D crystal and at every position and projects it onto a 2D plane, hence generating a library of 2D images corresponding to different rotation angles of the rotating 3D crystal. In real crystallisation monitoring, the on-line obtained 2D images try to match the stored 2D images, the 3D sizes of a real crystal is estimated as the digital 3D crystal corresponding to the matched 2D crystal stored in the library. (Wang et al., 2008) proposed to use two or more

synchronised cameras to firstly obtain two or three 2D images of the same moving crystal from different angles and then reconstruct its 3D shape from the 2D images using a 3D reconstruction algorithm. Bujak et al (Bujak and Bottlinger, 2008) used three orthogonal-configured cameras to measure particle's real 3D shape, though the system was designed for measuring dry particles of irregular shape rather than crystals in a slurry. Borchert et al. (Borchert et al., 2014) developed a method similar in principle to the camera model. It reconstructed the 3D crystal shape by comparing Fourier descriptors of the 2D crystal projections in pre-computed database with the Fourier descriptors of on-line measured 2D images. Mazzotti and co-workers (Kempkes et al., 2010; Schorsch et al., 2012) developed a clever method for measuring the 3D shape of crystals in slurry that passes a flow-through cell (though not directly in a stirred crystalliser): it uses a single camera but two mirrors to obtain two projections of the same particle. However, later, they improved the design by replacing the two mirrors with a second camera (Schorsch et al., 2014).

In our previous work, (Ma et al., 2015) presented a proof of concept study using stereo imaging for measuring crystal 3D shape. It employed two cameras that are fixed in an optimum angle and synchronised to take images and used a triangulation algorithm for 3D reconstruction. Based on a study on crystallisation of needle-shape crystals, β -form L-glutamic acid crystals, (Zhang et al., 2015) compared the performance of the stereo imaging technique with 2D imaging. It was found that 2D imaging greatly underestimated the crystal length. The triangulation algorithm for crystal 3D shape reconstruction has shown pretty robust performance for needle, plate and rod shaped crystals, but for crystals of more complicated structures, it can only correctly reconstruct 3D shape for a small proportion of crystals. The steps involved in stereo imaging based on a triangulation algorithm for 3D reconstruction are shown in Fig. 1.

All other steps in Fig. 1 are well established, but the fourth step in Fig. 1, i.e., the triangulation 3D shape reconstruction algorithm, requires identification of all the corners of a crystal on each of its 2D image, proving to be the weakest link. The images obtained on-line are often not perfect, as a result to identify all the corners of a crystal on its 2D projected image proved to be difficult. Therefore, a more robust reconstruction method, ideally not having to relying on full identification of all corners of a crystal in its 2D projections, needs to be developed.

In this paper, a new crystal 3D shape reconstruction method, a stereo imaging camera model, is presented. The main advantage is its robustness especially for crystals of complicated structures. In contrast to the above mentioned triangulation algorithm for 3D shape reconstruction that requires all the corners of a crystal to be identified on the 2D images, the stereo imaging camera model only requires the external boundaries of 2D images of a crystal. The method will be introduced by reference to potash alum crystallisation that produces crystals having 26 faces. The main difference from the camera model of Li et al (Li et al., 2006) and the work of (Borchert et al., 2014) lies in the fact that our model is based on stereo imaging while the early work was based on single camera 2D imaging. Stereo imaging camera model has a major advantage over the camera model based on 2D imaging, because the former captures the 3D shape information of an object while the later misses much of it. The principle of stereo imaging in here is similar to our 3D vision of human eyes. Our two eyes are separated by about 7cm. When looking at an object, the left and right eyes see slightly different images. Our brain calculates the real 3D image with these different left and right images. A 3D movie is made based on a similar principle, i.e., placing two cameras separating about the distance of two eyes, taking photographs at the same time. In the theatre, the left image of the movie and the right image are projected to the same screen by each projector with polarizing filters. 3D glasses that people wear when watching a 3D movie have

polarizing filters and allow movie projected from left projector to go into the left eye, and the movie projected from right projector to go into the right eye. In other words, the images taking by stereo imaging, in this work by two synchronised cameras arranged at an optimum angle, contains the 3D information of the object (here a crystal).

Details of the camera model based on stereo imaging for crystal 3D shape reconstruction will be presented in the next two sections. Application of the method to crystallisation of potash alum will be presented in section 4. Fig. 2 shows the morphology of a potash alum crystal. It has 26 faces, i.e. eight $\{111\}$, six $\{100\}$, and twelve $\{110\}$ faces. If symmetrical faces are treated as having identical characteristic dimensions, there will be three characteristic size dimensions, (x , y and z), representing the normal distances to $\{111\}$, $\{100\}$ and $\{110\}$ from the centre of the crystal.

2. The Stereo Imaging Camera Model for 3D Crystal Shape Reconstruction

Suppose we have a database about crystals of varied shape and size, for each crystal its shape and size is known. When a snapshot of a crystal (of unknown shape and size) in a real crystallizer is taken by a camera, we can compare this crystal with all the crystals in the database to find the most similar match in the database in terms of shape and size. Then the shape and size of the crystal in the database (we call it the matched crystal) is regarded as an estimate of the shape and size of the real crystal. This is the principle for crystal shape reconstruction based on a camera model. In the stereo imaging camera model two cameras are used. In the method, the key issues are: how the database of crystals of varied but known shape and size is created, and after a real crystal's photos are taken, how to find a crystal in the database that has the most similar shape and size. The database of crystals of varied but known shape and size is created on computer by rotating a digitised crystal in the three-dimensional space and varies the size dimensions in all face directions. At each size and

orientation, 2D projections of the crystal, according to the angles between the 2D cameras of the real stereo imaging instrument, are recorded. In order to describe the shape and size of a crystal, its contour information of the 2D images is processed to calculate Fourier descriptors and radius-based signature. The Fourier descriptors and radius-based signature are stored in the database. When the stereo imaging instrument captures 2D images of a real crystal during crystallization, the images are segmented to obtain the contour information and processed to obtain Fourier descriptors and radius-based information. To compare the real crystal with crystals in the database in terms of their similarity in shape and size, it is based on calculating a similarity measure called similarity distance (to be introduced later) using the Fourier descriptors. Below we introduce the details of the stereo imaging camera model.

The camera model, also called pinhole camera model by Li et al (Li et al., 2006), will be firstly introduced briefly before the camera model based on stereo imaging is described. In the pinhole camera model, a point in the object space with coordinates $\mathbf{X} = (X, Y, Z)^T$ is mapped to a point x with coordinates $(fX/Z, fY/Z, f)^T$ on the image plane. If the points from the object and image are represented by homogeneous vectors, the above projection can be simply expressed as a linear mapping between their homogeneous coordinates. The matrix multiplication relating the two sets of coordinates can be given as

$$\begin{pmatrix} X \\ Y \\ Z \\ 1 \end{pmatrix} \rightarrow \begin{pmatrix} fX \\ fY \\ Z \end{pmatrix} = \begin{bmatrix} f & 0 \\ f & 0 \\ 1 & 0 \end{bmatrix} \begin{pmatrix} X \\ Y \\ Z \\ 1 \end{pmatrix} \quad (1)$$

where f is the distance from camera centre to the image plane.

However, in the real situation, the relationship between the point in the 3D world and the corresponding point on an image can become much more complex than the above linear mapping. The general expression of the camera model can then be written as

$$\begin{pmatrix} X' \\ Y' \\ Z' \end{pmatrix} = \begin{pmatrix} p_{11}p_{12}p_{13}p_{14} \\ p_{21}p_{22}p_{23}p_{24} \\ p_{31}p_{32}p_{33}p_{34} \end{pmatrix} \begin{pmatrix} X \\ Y \\ Z \\ 1 \end{pmatrix} = P \begin{pmatrix} X \\ Y \\ Z \\ 1 \end{pmatrix} \quad (2)$$

where the matrix p is called calibration matrix of the camera, which includes the internal and external parameters of the camera. In our system, the original camera model was used only to project a 3D crystal to its 2D images. In this case, we are only concerned with the 2D projections obtaining via projecting the 3D polyhedral shape onto a plane. Therefore, a camera system is designed to ensure that the origin of the image coordinate system is the principal point so that the object coordinate system is the same as the camera coordinates, and distortion of camera lens can be ignored. Thus, Eq. (1) can be directly used as the camera model. The parameter f in Eq. (1) can be freely chosen because it only affects the size of the transformed image not its shape. It is worth noting that all coordinates should be transformed to a Cartesian coordinate system first. In this work we used such a camera system where the coordinates of a crystal can be obtained by rotating the crystal. The principle of the pinhole camera model will not be discussed in more detail here, since full details can be found in literatures (Hartley and Zisserman, 2003; Li et al., 2006).

The projection of an object (here a crystal) from a three-dimensional space onto a two-dimensional plane is a process in which one dimensional information of the object is lost (Hartley and Zisserman, 2003). In this study, the camera model based on stereo imaging was used to generate two 2D projections mimicking two cameras to capture two images with an angle. In this case, there is an extra constraint parameter, that is, the angle between two cameras. For the same object, real images and computed projections from different angles in database could be correspondent to each other. Compared to a single camera model, more shape information from projections can be captured, which is beneficial to minimising errors in identifying the 3D shape and size of a crystal. The detailed algorithm of the method will be described in the following sections.

3. 2D Projection Contour

Digitised 3D Crystal Shape

The morphology of a crystal can be estimated in advance according to its crystallography and morphology. The morphology of a crystal can be defined by the locations of all planes, i.e., normal distances from the faces to the crystal centre, and the interfacial angles between the planes, (see Fig. 2). In a 3D coordinate space, a crystal face can be represented by Miller indices (hkl), the unit cell axes a, b and c, and the angles between them. The 3D shape of a polyhedral convex crystal is described by a group of linear inequalities:

$$Nv \leq H \quad (3)$$

where v is the 3×1 vector of coordinates on a plane, N is a $w \times 3$ matrix with the unit normal of the w faces. The unit normal N to the plane is oriented from the centre to the plane and can be calculated by the crystallographic axes and the Miller indices of the crystal system (Borchert et al., 2014; Schwarzenbach, 1997; Zhang et al., 2006). H is also a $w \times 1$ matrix, which contains the normal distance of each face.

The convex hull of the polyhedron is composed of faces, edges and vertices. The edges and vertices on the crystal surface are made up of faces, more specifically, the intersection of two faces generates edge, and the junction of three or more faces produces vertex. In this study, only 3D size of crystal evolution was studied without considering the variation of crystal habit, that is, there is no appearance or disappearance of crystal faces. Therefore, we will focus on the vertices. Actually, the shape of a crystal is known when the coordinates of all vertices are obtained, because the vertices are composed of convex combinations, called V-representation (Borchert and Sundmacher, 2012; Ziegler, 1995). Based on Eq. (3), the coordinates of a vertex can be defined by the corresponding equalities.

$$V = N^{-1}H \quad (4)$$

where V stands for the crystal vertices.

Crystal Rotation

When all coordinates are transformed into a Cartesian coordinate system, the method of rotating a 3D crystal in a camera model is essentially the same as the rotation of the reference system along the Euler angles δ , θ and φ . The two dimensional projection matrix can be obtained through the following matrix multiplication (Borchert et al., 2014; Eggers, 2008; Korn and Korn, 2000).

$$P_i = PV \quad (5)$$

$$P = P_1 P_2 =$$

$$\begin{bmatrix} 1 & 0 & 0 \\ 0 & 1 & 0 \end{bmatrix} \times \begin{bmatrix} \cos \delta & -\sin \delta & 0 \\ \sin \delta & \cos \delta & 0 \\ 0 & 0 & 1 \end{bmatrix} \times \begin{bmatrix} 1 & 0 & 0 \\ 0 & \cos \theta & -\sin \theta \\ 0 & \sin \theta & \cos \theta \end{bmatrix} \times \begin{bmatrix} \cos \varphi & -\sin \varphi & 0 \\ \sin \varphi & \cos \varphi & 0 \\ 0 & 0 & 1 \end{bmatrix} \quad (6)$$

where P_i ($i = 1, 2, \dots$) are vertices of a crystal projection on the 2D plane. To include as many orientations as possible during the rotation operation, the values of δ and φ are selected randomly from a uniform distribution between 0 and 2π , i.e.:

$$0 \leq \delta < 2\pi \quad (7)$$

$$0 \leq \varphi < 2\pi \quad (8)$$

However, in order to ensure an equal probability for all directions, θ is taken as the arcsine of a number m , which is randomly distributed in the range between -1 to 1, i.e.:

$$\theta = \arcsin(m), -1 \leq m < 1 \quad (9)$$

In this study, the value of θ was chosen randomly from 0 to π . The same crystal can generate many different 2D projections with different random combinations of the angles δ , θ and φ . Moreover, the number of rotation depends on the interval of two neighbouring angles.

The 2D shape of the projections may only change very little at a very small step, and the

generation process of 2D projections is time-consuming and costly. On the other hand, the large rotation step may cause loss of accuracy. It is worth mentioning that the minimum degree at which the crystal needs to be rotated is dependent on the complexity of the 3D crystal and the initial position of the rotation. In the current study, the rotating step for three Euler angles was selected to be 10° . There are two cameras that are fixed at an optimum angle in the on-line stereovision imaging system, thus two databases could be generated corresponding to the two cameras in order to conveniently compare with on-line images. The number of total orientations in each database based on the above rotation steps is $36 \times 18 \times 36$, which leads to $2 \times 36 \times 18 \times 36$ 2D projections being generated in the database library. To better match projections (images) in the database with on-line images obtained from on-line imaging instrument, the same angle as the optimum angle between two real-cameras was used for the generation of two databases for the two virtual cameras using the camera model. In addition, the particle is observed from the Z-axis of the rotated coordinates. Therefore, when two databases have the same δ and φ , the difference of rotation angle between two databases is from the Z-axis direction, i.e., θ .

To obtain the information of the 2D projection boundary, some properties of the projection should be computed according to the vertices of the projected crystal. The area A and the coordinates of the centroid (X_c , Y_c) can be calculated using the coordinates of the n_j vertices in the convex hull with the equations below. The vertices are ordered in a counter clockwise direction (Bockman, 1989; Borchert et al., 2014; Burger, 2008; Eggers, 2008):

$$A = \frac{1}{2} \sum_{i=1}^{n_j} (X_i Y_{i+1} - X_{i+1} Y_i) \quad (10)$$

$$X_c = \frac{1}{6A} \sum_{i=1}^{n_j} (X_i + X_{i+1})(X_i Y_{i+1} - X_{i+1} Y_i) \quad (11)$$

$$Y_c = \frac{1}{6A} \sum_{i=1}^{n_j} (Y_i + Y_{i+1})(X_i Y_{i+1} - X_{i+1} Y_i) \quad (12)$$

where $(X_{n_i+1}; Y_{n_i+1}) = (X_1; Y_1)$, the linear connection of between the neighbouring vertices forms the contour of the projection.

Shape Descriptors

Signature of a 2D Projection

Shape descriptors are often used to capture the shape characteristics of an object, some types have physical meanings such as aspect ratio and roundness, some are latent such as principal component analysis (PCA) based shape descriptors (Zhang and Lu, 2004; Zhang et al., 2016). In this work, shape Fourier descriptors (FDs) were used. FDs can be calculated from shape boundary signatures, either curvature, or radius, or boundary coordinates. It was found in literature that the three methods for calculating the signatures do not show meaningful differences in shape classification (Lu and Sajjanhar, 1999). In this study, radius-based signature was chosen as index for FDs.

Radius-based signature consists of a number of ordered distances from the shape centroid to the boundary points (called radii), which can be expressed by the following equation (Li et al., 2006):

$$r_i = \sqrt{(X_i - X_c)^2 + (Y_i - Y_c)^2} \quad (i = 0, 1, 2 \dots K - 1) \quad (13)$$

where r_i is the distance from the shape centroid (X_c, Y_c) to the i^{th} boundary signature point (X_i, Y_i) , K is the number of the sampling points. In our system, 128 uniformly sampled boundary points were taken in the range from 0 to 2π . Thus 128 radii ordered in an anticlockwise orientation were used as the shape signature. Additionally, the starting and end points on the boundary are the radii corresponding to 0 and 2π of the angle, respectively. It is difficult to obtain the radii of sampling points if Eq. (13) is directly used, as the Cartesian coordinates (X_i, Y_i) were unknown except for the vertices of the convex polygon. However, we can transform a linear equation (Eq. (14)) which can be deduced by coordinates of two points $((X_i,$

Y_i) and (X_{i+1}, Y_{i+1})) determined by the coordinates of the successive vertices to a polar expression (Eq. (16)) based on the relationship between the Cartesian and the polar coordinate system (Eq. (15)).

$$Y - Y_i = \frac{Y_{i+1} - Y_i}{X_{i+1} - X_i} (X - X_i) \quad (14)$$

$$X = r \cos \varepsilon; Y = r \sin \varepsilon \quad (0 \leq \varepsilon \leq 2\pi) \quad (15)$$

$$r(\varepsilon) = \frac{X_{i+1}Y_i - X_iY_{i+1}}{(X_{i+1} - X_i)\sin\varepsilon - (Y_{i+1} - Y_i)\cos\varepsilon} \quad (16)$$

where ε is the angle between the ray that linearly connects the origin and point, and X-axis. Because these sampled signatures were uniformly distributed between two neighbouring vertices on the projection boundary, Eq. (16) can be used to calculate the radii based on known angle corresponding to sampling points.

Signature of Real Images

For the signature of the projection boundary, details have been discussed in the above section. However, in the real situation, the image from an imaging system can be recorded only at a finite resolution on a CCD-chip, which means that the boundary is composed of a set of mean discretized pixel coordinates (see Fig. 3). In Fig. 3, X and Y represent the axes in the pixel coordinate system, and x_c is the centre of a particle's projection. The distance $r(\varepsilon)$ (from the centre to a point on the boundary, see Eq. (16)) and the angle ε (in the range from 0 to 2π) are the polar coordinates of a point A (the intersection between the ray from the centre (line 2) and the linear connecting line of neighboring pixel points (line 1)). $k_{i-1}, k_i, k_{i+1}, k_{i+2}, k_{i+3}$ are the pixel points on the boundary of the particle's projection. As shown in Fig. 3, point A is on the connecting lines between two continuous pixel points (k_i, k_{i+1}). In order to calculate the distance ($r(\varepsilon)$), these pixel points on the boundary were assumed as the vertices of the convex polygon. In this way, when there existed some sampled points locating between the two

neighbouring pixel points, Eq. (16) can be used to evaluate the distance from the centre of the image to these points. It is worth noting that the pixel coordinates should be transformed into a Cartesian system beforehand. Therefore, for point A, the coordinates $(X_{i+1}, Y_{i+1}; X_i, Y_i)$ in Eq. (16) represent the pixel points (k_{i+1}, k_i) corresponding to Cartesian coordinates. While when the points were just pixel points on the boundary, the distances from the centre to these points can be directly obtained using Eq. (13). To reduce the error in the comparison process at a later stage, the 128 sampled points were also equally distributed in the interval between 0 to 2π , as well as the predefined signatures on the boundary of the projections.

Fourier Transform

The radius-based signature can be a good representation index of the object shape. It can precisely describe the size of an object. This method may be effective in terms of the objects with the same shape. Because the objects with different shapes may have similar radius signature, it is difficult to recognise them in this case. Therefore, alternative methods are needed to represent and distinguish the properties of objects, especially size and shape. For instance, a potash alum crystal having 26 faces can project different convex polygons during rotation, such as hexagon, octagon, and dodecagon. Obviously, only relying on the radius signature may not fulfil the requirements of discriminating them. Generally, the crystal shape is not growing uniformly due to the influence of external factors. Moreover, the images recorded by a camera may have finite resolution, and in some cases, they are blurring, hence the contour of an image may not represent the features of real crystals.

The Fourier descriptors as a general method are most extensively applied in the description and discrimination of boundary curves. Fourier descriptors have some important properties, such as translation invariance, scale and rotation invariant. Therefore, FDs have been employed for pattern recognition, shape discrimination and hand print character recognition

of plane closed curves due to these advantages (Borchert et al., 2014; Granlund, 1972; Li et al., 2006; Persoon and King-Sun, 1977; Zahn and Roskies, 1972). The Fourier descriptors based on the shape radii are given by (Gonzalez and Woods, 2008)

$$F_n = \sum_{i=0}^{K-1} r_i \exp\left(-\frac{2\pi j n i}{K}\right), \quad i = 0, 1, \dots, K-1 \quad (17)$$

The FDs acquired in this way is translation invariant due to the translation invariance of the shape radii. To achieve the orientation invariance of the shape description, only the magnitude of the Fourier coefficients is taken into account (Borchert et al., 2014):

$$|F_i| = \sqrt{R_e(F_i)^2 + I_m(F_i)^2}, \quad i = 1, \dots, K-1 \quad (18)$$

In order to obtain scale invariance, the Fourier coefficients are resized by the division of the largest one ($\max(F_i)$). The final Fourier descriptors can be expressed as

$$FD_i = \frac{|F_i|}{\max(F_i)} \quad (19)$$

In the descriptors, the information of the general shape is in the low frequency descriptors while the information about smaller details is in the higher frequency descriptors. In here, we define a similarity distance (SD), calculated by Eq. (20), to quantify the closeness of a matching between two images.

$$SD = \left(\sum_{i=1}^K (FD_{1,i} - FD_{2,i})^2\right)^{1/2} \quad (20)$$

where $FD_{1,i}$ and $FD_{2,i}$ stand for the i^{th} Fourier descriptor of the images 1 and 2, respectively, K is the number of the Fourier descriptors used to represent the shape. The smaller the similarity distance SD , the more similar the two images are.

Database Size

Accurate estimation of a crystal's multidimensional sizes by the matching method depends not only on the quality of the captured images, but also on the discretisation steps of the

orientation angles and crystal sizes during the generation of the database, and the later decides the size of the database. The smaller the discretisation steps, the higher the matching accuracy, but the bigger the size of the database, hence longer CPU time to generate the database. In this study, three size characteristic parameters of the potash alum crystals were chosen to be from 50 μm to 500 μm with the step size being 10 μm . As we known, the potash alum crystal has 26 faces. The disappearance of one or two of the three faces $\{111\}$, $\{100\}$ and $\{110\}$ may result in seven possible morphological forms (Wan et al., 2009). In the simulations to generate the database, to ensure that all the crystals have 26 faces, there are additional constraints based on the area of the feature faces, i.e., their areas should not be zero when calculating with the equations from the previous paper (Ma et al., 2008). Overall, there are 8325 combinations of three characteristic parameters (x , y , z) using the selected size range and step size for the database. The choice of orientation and sampling points were discussed in sections Crystal Rotation and Shape Descriptors. Therefore, the database was generated based on the following settings: $n_{x,y,z}=8325$, $n_{\delta,\theta,\varphi}=23328$ and $K=128$. Furthermore, the combination of two cameras with a stereo angle can also improve the accuracy of matching result, the details will be discussed in later sections.

Shape Estimation Principle

Fig. 4 demonstrates the scheme of crystal shape estimation (matching). Each 3D crystal with the 23328 orientations was projected as 23328 2D shapes using the camera model, hence 23328 computer-generated 2D images. This corresponds to the same number of Fourier descriptors in each database for future matching with real images. In the database, each set of FDs represents a 2D shape of the crystal under one orientation. Once on-line images are available, their FDs will be first calculated. Then the most similar 2D shape in the database

will be found through comparing the similarity distance values, calculated by Eq. (20), between the image acquired on-line and the computer-generated images in the database.

Sometimes the 2D projections of a crystal in the database may be very similar from two successive steps. This is challenging in finding the matching result between the database and the on-line images by the instrument. To solve this issue, we can firstly choose the top five of 2D shape with the highest similarity (i.e. smallest SD values) as targets in each matching process. With the identification of the top five marked 2D shapes in the database, the corresponding normal distances of individual faces can be obtained from the records when generating the database. It is noted that the normal distances obtained in here were not the final 3D size of crystal but a rough estimate.

The experimental set up is shown in Fig. 5. Crystals lie at the bottom of the reactor and grow under the observation of the stereo imaging instrument. Fig. 6 shows an example, in which Fig. 6 (a) and Fig. 6 (b) are real images taken by camera 1 and camera 2 at time 1s, and the white areas of (c) and (d) are their image segmentation results. Figs. 6 (e) and (f) are real images taken by cameras 1 and 2 at time 3600s, and the gray areas in (c) and (d) are their image segmentation results. The real images were processed using the multi-scale image analysis software of PharmaVision Ltd, SHAPE, which was reported in (Calderon De Anda et al., 2005b) and (Wan et al., 2008). The edge detection is based on gradient change of intensity of an image. After edge detection, morphological closing is the next step to close the breaks in features. In terms of the continuity of borders, these continuous pixel points on the boundaries of particles' projection in the images were kept, while discontinuous pixel points were removed in the image process. In this particular experiment, the crystal remained having twelve edges, and crystal growth mainly changed the size, and the shape change - the relative size of each edge, is very small. Since FDs with scale invariant mainly discriminate shape difference of objects, the radii data that captures size information is combined with FDs.

Because the crystal is static, the 2D shape in real images can be captured at a specific orientation. Based on this concept, it is assumed that the radii of 2D shapes from a crystal are proportional to 3D size of the crystal. Actually, two stages were used to reconstruct the 3D shape of a crystal in this process: 1) the SD between the Fourier descriptors of real images and 2D projections in the data base is calculated so that we can find the most similar projections from the database with the shape in the real image. Meanwhile, the initial 3D size of the crystal corresponding to the most similar projections can be obtained, which may be not unique; 2) the radii ratio between of the most similar projections obtained in the first step and real images were then employed to determine the final 3D size of the crystal. Hence, the initial 3D size of a crystal may not be the final size. Only when the radii ratio is close to one, the initial 3D size can be considered as the final size of the crystal.

4. Experiments

Materials

Potassium (potash alum), $\text{KAl}(\text{SO}_4)_2 \cdot 12\text{H}_2\text{O}$, has four molecules in the cubic unit cell with a space group of $\text{Pa}\bar{3}$ and cell parameters of $a = b = c = 12.517\text{\AA}$ and $\alpha = \beta = \gamma = 90^\circ$. Potash alum crystals can be easily grown from aqueous solutions and the morphology (see Fig. 2) is dominated by the large octahedron face $\{111\}$ and two essential but considerably smaller faces, the cubic face $\{100\}$, and the rhomb-dodecahedron face $\{110\}$ (Klapper et al., 2002; Ma et al., 2008; Ristic et al., 1996; Ristic et al., 1997). Three minor faces, $\{221\}$, $\{112\}$ and $\{012\}$, that exist only at early stages during crystallisation and disappear quickly, hence, have not been frequently observed. These three primary growth forms are manifested in the external morphology through the multiplicities associated with the cubic symmetry which yields a total of 26 crystal growth surfaces, i.e., eight $\{111\}$, six $\{100\}$ and twelve $\{110\}$

faces as three feature faces. As shown in Fig. 2, x, y and z stand for the normal distances from geometric centre to three feature faces, respectively.

The solubility of potash alum crystals can be estimated by Eq. (21) (Barrett and Glennon, 2002; Nollet et al., 2006), and the relative supersaturation can be calculated by Eq. (22).

$$\ln(s)=12.1/T+10.47\ln(T)-65.73 \quad (21)$$

$$\sigma = C/C^*-1 \quad (22)$$

where s is solute mole fraction, σ is the relative supersaturation, T is the temperature in Celsius, C is the concentration and C* is the solubility in g/L. The solid potash alum crystals were purchased from Sigma-Aldrich International Ltd.

Calibration Experiments and Models

Attenuated total reflectance-Fourier transform infrared (ATR FTIR) instrument, ReactIR 4000 from Mettler Toledo Ltd was employed to monitor the solution concentration in real time in the cooling crystallization process. Calibration experiments were carried out to collect data for predictive model development. The data contains 30 spectra (Table 1), corresponding to solutions at temperatures of 10, 20, 30, 40 and 50°C, and concentration range from 2 to 24 g/100g water. The peaks at the wave numbers of 1100 cm⁻¹ and 1640 cm⁻¹ are associated with potash alum sulphate (SO₄²⁻) and the H-O-H in water.

Partial least square regression (PLS) (Ma and Wang, 2012a; Ma and Wang, 2012b; Wold et al., 2001) was used to develop the concentration predictive model. The calibration data, as shown in Table 1, comprises the input variables, i.e. the wave numbers in the range between 800 cm⁻¹ to 1800 cm⁻¹ at 4 cm⁻¹ interval (The IR spectra peak of potash alum is known to be at the wave numbers of 1100 cm⁻¹ and 1640 cm⁻¹) and temperature, and the output variable i.e. the solution concentration. Although it was found the influence of temperature on spectra absorbance is not as obvious as solution concentration, temperature was still used as an input

variable. The data was divided into two sets, the training dataset (18 spectra) for calibration model development and the test dataset (12 spectra) for model verification. The model was built using PLS (partial least squares). R^2 and RMSEP (root mean square of prediction) for the training data are $R^2=0.9965$, RMSEP = 0.091 g/100g water. For the test data, $R^2=0.9987$, RMSEP = 0.088 g/100g water.

Crystallisation Experiments

The 200mL reactor used for the cooling crystallisation experiments is shown in Fig. 5. A Julabo FP50-HE thermostatic bath controls temperature by manipulating the water circulation. The temperature was measured using a platinum resistance thermometer (PT100). Solution concentration was measured using the ATR FTIR instrument (ReactIR 4000).

The on-line imaging system depicted in Fig. 5 is the non-invasive on-line 3D imaging instrument Stereovision^{NI} of (PharmaVision (Qingdao) Ltd). It consists of two Basler avA1000-120km CCD cameras (camera 1 and camera 2) and two 2x optic lenses. The camera fitted with Truesense Imaging sensor has a field of view with 2.82 mm×2.82 mm and can carry out image acquisition with a pixel resolution of 1024×1024 under a maximum frequency of up to 120 images per second. In this study, the imaging speed was selected as one image per second. A ring LED light source was used to provide illumination. The Stereovision^{NI} acquisition software was used for acquisition, storage and management of the images. The relative measurement error is less than 2%.

Saturated solution at 30°C was prepared with 32.8 g of potash alum and 200 mL of fresh distilled water. The solution was heated quickly to 40°C and held at the temperature for an hour until the solid was completely dissolved. The solution was then cooled down to 30°C at a relatively fast cooling rate of 1°C/min and maintained at 30°C for half hour. Next, the solution was cooled down to 28°C at a slow cooling rate of 0.05°C/min. At the temperature of 28°C, 0.6 g of seeds (2% of the solute (Chung et al., 1999; Kubota et al., 2001)) were added

to the supersaturated solution. After that, the solution was cooled down at a cooling rate of $0.05^{\circ}\text{C}/\text{min}$ for one hour. The addition of seeds in the cooling crystallisation process is to inhibit the secondary nucleation and the formation of tiny crystals. Observation and recording of process operation conditions (concentration and supersaturation) were conducted in real-time, as shown in Fig. 7. Obviously, the growth of potash alum crystals happened with the decrease of the solute temperature during the cooling crystallisation. For the estimation of crystal shape, the temperature range used was from 28 to 25°C and the corresponding relative supersaturation range was from 0.12 to 0.26.

5. Results and Discussion

Image Analysis

The multi-scale image analysis software of PharmaVision Ltd, SHAPE, was used to extract crystals from the image background. Key part of the image segmentation algorithms was published in (Calderon De Anda et al., 2005b; Wan et al., 2008) so will not be repeated here. The segmented images were stored in the format of pixel coordinates, i.e., all the points on the images including sampling signature were the pixel coordinates, which cannot be used to directly calculate the FDs. The pixel coordinates were then transformed to the Cartesian coordinates based on the magnification (2x) and the size of each pixel (pixelated images with a resolution of $5.5\ \mu\text{m}/\text{pixel}$).

Reconstruction of Crystal 3D Shape

The potash alum crystallisation experiment lasted for one hour, one image was taken every second, so 3600 images in total were recorded. The SD (similarity distance, defined by equation (20)) values calculated based on single cameras and stereo imaging at different times are plotted in Fig. 8. It needs to point out that a SD value describes how similar it is

between the crystal matched in the database and the imaged real crystal, the smaller the SD value, the more similar. Ideally, the SD is calculated with the real 3D shape of the crystal, unfortunately the real 3D shape is unknown in a real crystallisation experiment.

Fig.8 shows that SD values using stereo imaging camera model are well below 0.02 while the SD value obtained by a single camera (camera 1 or camera 2) is almost above 0.03.

Table 2 shows at three time points, 0, 1800 and 3200 seconds, the 2D images captured by the two cameras and the reconstructed 3D shape of a crystal. It can be seen from Table 2 that the accuracy of shape estimation is higher using stereo camera to match the online images with database images. Furthermore, the SD is about 50% smaller when stereo camera was employed. Taking a pair of images at the 1800th s as an example, the SD are 0.0403 and 0.0398 using single camera 1 and single camera 2, respectively. However, the SD is only 0.0297 using stereo camera.

Fig. 9 shows the normal distances of face {111} reconstructed. It can be seen that the variation of the normal distances obtained using stereo imaging (blue triangles) with time is more stable. In contrast, the curves (red circles (camera 1) and black squares (camera 2)) using a single camera showed strong oscillations.

In Fig.9, at sampling time 3400th second, there is a noticeable drop in the red curve (camera 1). Every step involved in calculating this point is examined. The steps involved are: (1) camera 1 took an image of the crystal at 3400s, (2) the image was processed for segmentation of the crystal from the image background, (3) Fourier descriptors were calculated, (4) Use equation (20) to calculate a similarity distance (SD) characterising the similarity of the real crystal with each crystal of known shape and size in the database, the crystal in the database that gives the smallest similarity distance is the matched crystal, (5) the corresponding 3D shape and size of the matched crystal is considered as the 3D shape and size of the real crystal.

It needs to bear in mind that the shape of the real crystal, and the shape of a crystal in the database is described by Fourier descriptors (FDs), and FDs of a crystal's shape is not 100% the real shape of the crystal, it is an approximate description of the crystal's shape. Now it is clear that the approach does not guarantee that the crystal in the database that has the closest shape and size with the real crystal be found. In the case of the abnormal point of 3400th second in Fig. 9, based on SD values, the method of using camera 1 only did not match the right crystal - it matched a much smaller crystal than the right one. But how did we know which is the right crystal in the database? We knew it because we were continuously monitoring the crystal's growth, we knew its size and shape before 3400th second and after 3400th second, so were pretty sure what should be the right shape and size at the 3400th second. We examined the image captured at 3400s by camera 1 and the image segmentation, there were no abnormalities. Despite no abnormalities in steps 1 (imaging taking) and 2 (image segmentation), it still the matched a very small crystal that gives the smallest SD, 0.0312. But at the 3400s, the stereo imaging camera model, found the most likely correct crystal, further demonstrating the advantage of the stereo imaging camera model in this paper. For the most likely correct crystal in the database, camera 1 calculated a SD value of 0.0365, larger than 0.0312. Actually 0.0365 is the second smallest SD.

Estimation of Facet Growth Kinetics

Fig. 10 shows the distributions of normal distances (x , y , and z) of three individual faces, $\{111\}$, $\{100\}$ and $\{110\}$, given by Eqs. (23), (24) and (25). As can be seen from Fig. 10 (a), the normal distances of individual faces increase with time, t , and a second order polynomial function was used to curve-fit them with R^2 being over 0.99:

$$x = 82.01 + 0.00989t + 2.2072 \times 10^{-6}t^2 \quad (23)$$

$$y = 65.12 + 0.00529t + 2.4571 \times 10^{-6}t^2 \quad (24)$$

$$z=100.49+0.01021t+3.6191\times 10^{-6}t^2 \quad (25)$$

The growth rates of three characteristic faces were calculated using Eqs. (23)-(25) as negative values of growth rates may be produced when the estimated data were directly applied. The obtained growth rates have a linear relationship with time as shown in Fig. 10 (b). Fig. 11 shows the 3D shape evolution of a potash alum crystal based on the normal distances of three individual faces in Fig. 10 (a).

The solution concentration, solubility and the relative supersaturation are illustrated in Fig. 7. Based on Eqs. (23)-(25) and the relationship between the relative supersaturation and crystallisation time, the crystal growth rates of three individual faces against the relative supersaturation (Fig. 12) can be expressed by the following equations:

$$v_{\{111\}}=(0.1822\sigma -0.0168) \times 10^{-6} \quad (26)$$

$$v_{\{100\}}=(0.2029\sigma -0.0244) \times 10^{-6} \quad (27)$$

$$v_{\{110\}}=(0.2988\sigma -0.0335) \times 10^{-6} \quad (28)$$

where v represents the growth rate of individual faces in m/s. It is clear from Fig. 12 that the growth rates of three individual faces have a linear relationship with the relative supersaturation in the range from 0.12 to 0.26. In addition, when the relative supersaturation is less than 0.15, the growth of face $\{111\}$ is the fastest. However, once the relative supersaturation is over 0.15, the growth rate of face $\{110\}$ is the largest with the growth rates of face $\{111\}$ and face $\{100\}$, slowly approaching each other with the further increase of the relative supersaturation. In the current study, growth rates of potash alum crystals in three individual face directions obtained at the relative supersaturation between 0.12 and 0.26 have the similar trend to and the same order of magnitude with the literatures (Hilgers and Urai, 2002; Nollet et al., 2006). Although the growth rates of three individual faces have been presented in previous experiments, there did not provide reliable experimental data for $\{110\}$ and $\{100\}$ faces in literature. Normally, the growth rates of these two faces were estimated

based on ratios with the growth rate of face {111} (Klapper et al., 2002) or predicted using the morphological population balance (Ma et al., 2008) with the effect of growth rate dispersion. It is worth noting that the method presented in this study can be used to estimate not only the growth rate of face {111} of potash alum crystals, but also the growth rates of other two faces, {100} and {110}, which are much more difficult to obtain. Furthermore, the solution concentration was directly measured using on-line ATR FTIR instrument in the crystallisation process, thus the relationship between growth rates of individual faces and the relative supersaturation was obtained.

6. Conclusion

A stereo imaging camera model approach for 3D shape reconstruction of complex crystal structures was introduced. Compared to a previous approach for crystal 3D shape reconstruction - the triangulation algorithm that requires all the corners of a crystal to be found on its 2D projections, the current method only requires the external boundaries of the 2D projected image of the crystal. Application of the new method to the crystallisation of potash alum showed that it is more accurate than the previously reported camera model based on a single 2D camera. The work also demonstrated that combined use of 3D imaging and ATR FTIR can derive crystal facet growth kinetics.

Acknowledgments

Financial supports from the China One Thousand Talent Scheme, the National Natural Science Foundation of China (NNSFC) under its Major Research Scheme of Meso-scale Mechanism and Control in Multi-phase Reaction Processes (project reference: 91434126), the Natural Science Foundation of Guangdong Province (project title: Scale-up study of protein crystallisation based on modelling and experiments, project reference: 2014A030313228) as well as the Guangdong

Provincial Science and Technology Projects under the Scheme of Applied Science and Technology Research Special Funds (Project Reference: 2015B020232007) are acknowledged. The authors would like to extend their thanks to Pharmavision (Qingdao) Intelligent Technology Limited (www.pharmavision-ltd.com) for providing the non-invasive on-line 3D imaging instrument Stereovision^{NI}. Thanks are also due to the Oversea Study Program of Guangzhou Elite Project (GEP) in China for providing the first author a scholarship allowing him to carrying out visiting PhD research at the University of Leeds.

References

- Barrett, P., Glennon, B., 2002. Characterizing the Metastable Zone Width and Solubility Curve Using Lasentec FBRM and PVM. *Chemical Engineering Research and Design* 80, 799-805.
- Bockman, S.F., 1989. Generalizing the formula for areas of polygons to moments. *Am. Math. Monthly* 96, 131-132.
- Borchert, C., Sundmacher, K., 2012. Efficient formulation of crystal shape evolution equations. *Chemical Engineering Science* 84, 85-99.
- Borchert, C., Temmel, E., Eisenschmidt, H., Lorenz, H., Seidel-Morgenstern, A., Sundmacher, K., 2014. Image-Based in Situ Identification of Face Specific Crystal Growth Rates from Crystal Populations. *Crystal Growth & Design* 14, 952-971.
- Bujak, B., Bottlinger, M., 2008. Three-Dimensional Measurement of Particle Shape. *Particle & Particle Systems Characterization* 25, 293-297.
- Burger, W., 2008. *Digital Imaging Processing-An Algorithmic Introduction Using Java*, first ed. Springer, New York.
- Calderon de Anda, J., Wang, X.Z., Lai, X., Roberts, K.J., 2005a. Classifying organic crystals via in-process image analysis and the use of monitoring charts to follow polymorphic and morphological changes. *Journal of Process Control* 15, 785-797.
- Calderon De Anda, J., Wang, X.Z., Roberts, K.J., 2005b. Multi-scale segmentation image analysis for the in-process monitoring of particle shape with batch crystallisers. *Chemical Engineering Science* 60, 1053-1065.
- Chung, S.H., Ma, D.L., Braatz, R.D., 1999. Optimal seeding in batch crystallization. *The Canadian Journal of Chemical Engineering* 77, 590-596.
- Eggers, J., 2008. *Modeling and Monitoring of Shape Evolution of Particles in Batch Crystallization Processes*. PhD thesis, ETH Zürich.
- Gonzalez, R.C., Woods, R.E., 2008. *Digital Image Processing*, 3rd ed. Prentice Hall.
- Granlund, G.H., 1972. Fourier Preprocessing for Hand Print Character Recognition. *Computers, IEEE Transactions on C-21*, 195-201.

- Hartley, R., Zisserman, A., 2003. Multiple view geometry in computer vision, second ed. Cambridge University Press, Cambridge.
- Hilgers, C., Urai, J.L., 2002. Experimental study of syntaxial vein growth during lateral fluid flow in transmitted light: first results. *Journal of Structural Geology* 24, 1029-1043.
- Huo, Y., Liu, T., Liu, H., Ma, C.Y., Wang, X.Z., 2016. In-site crystal morphology identification using imaging analysis with application to L-glutamic acid crystallization. *Chemical Engineering Science* 148, 126-139.
- Kempkes, M., Vetter, T., Mazzotti, M., 2010. Measurement of 3D particle size distributions by stereoscopic imaging. *Chemical Engineering Science* 65, 1362-1373.
- Klapper, H., Becker, R.A., Schmiemann, D., Faber, A., 2002. Growth-Sector Boundaries and Growth-Rate Dispersion in Potassium Alum Crystals. *Crystal Research and Technology* 37, 747-757.
- Korn, T.M., Korn, G.A., 2000. *Mathematical handbook for scientists and engineers: definitions, theorems, and formulas for reference and review*, book, 2nd Revised edition. Dover Publications, New York, page 475.
- Kubota, N., Doki, N., Yokota, M., Sato, A., 2001. Seeding policy in batch cooling crystallization. *Powder Technology* 121, 31-38.
- Larsen, P.A., Rawlings, J.B., 2009. The potential of current high-resolution imaging-based particle size distribution measurements for crystallization monitoring. *AIChE Journal* 55, 896-905.
- Larsen, P.A., Rawlings, J.B., Ferrier, N.J., 2006. An algorithm for analyzing noisy, in situ images of high-aspect-ratio crystals to monitor particle size distribution. *Chemical Engineering Science* 61, 5236-5248.
- Li, R.F., Thomson, G.B., White, G., Wang, X.Z., Calderon de Anda, J., Roberts, K.J., 2006. Integration of crystal morphology modeling and on-line shape measurement. *Aiche Journal* 52, 2297-2305.
- Lovette, M.A., Browning, A.R., Griffin, D.W., Sizemore, J.P., Snyder, R.C., Doherty, M.F., 2008. Crystal shape engineering. *IndustrialEngineeringChemistryResearch* 47, 9812-9833.
- Lu, G., Sajjanhar, A., 1999. Region-based shape representation and similarity measure suitable for content-based image retrieval. *Multimedia Systems* 7, 165-174.
- Ma, C.Y., Liu, J.J., Wang, X.Z., 2015. Stereo imaging of crystal growth. *AIChE Journal* 62, 18-25.
- Ma, C.Y., Liu, J.J., Wang, X.Z., 2016. Measurement, modelling, and closed-loop control of crystal shape distribution: Literature review and future perspectives. *Particuology* 26, 1-18.
- Ma, C.Y., Wang, X.Z., 2012a. Closed-loop control of crystal shape in cooling crystallization of l-glutamic acid. *Journal of Process Control* 22, 72-81.
- Ma, C.Y., Wang, X.Z., 2012b. Model identification of crystal facet growth kinetics in morphological population balance modeling of L-glutamic acid crystallization and experimental validation. *Chemical Engineering Science* 70, 22-30.
- Ma, C.Y., Wang, X.Z., Roberts, K.J., 2008. Morphological population balance for modeling crystal growth in face directions. *Aiche Journal* 54, 209-222.
- Nollet, S., Hilgers, C., Urai, J.L., 2006. Experimental study of polycrystal growth from an advecting supersaturated fluid in a model fracture. *Geofluids* 6, 185-200.

- Patience, D.B., Rawlings, J.B., 2001. Particle-shape monitoring and control in crystallization processes. *AIChE Journal* 47, 2125-2130.
- Persoon, E., King-Sun, F., 1977. Shape Discrimination Using Fourier Descriptors. *Systems, Man and Cybernetics, IEEE Transactions on* 7, 170-179.
- PharmaVision(Qingdao)Ltd, www.pharmavision-ltd.com, accessed September 2016.
- Ristic, R.I., Shekunov, B., Shewood, J.N., 1996. Long and short period growth rate variations in potash alum crystals. *Journal of Crystal Growth* 160, 330-336.
- Ristic, R.I., Shekunov, B.Y., Sherwood, J.N., 1997. The influence of synchrotron radiation-induced strain on the growth and dissolution of brittle and ductile materials. *Journal of Crystal Growth* 179, 205-212.
- Schorsch, S., Ochsenein, D.R., Vetter, T., Morari, M., Mazzotti, M., 2014. High accuracy online measurement of multidimensional particle size distributions during crystallization. *Chemical Engineering Science* 105, 155-168.
- Schorsch, S., Vetter, T., Mazzotti, M., 2012. Measuring multidimensional particle size distributions during crystallization. *Chemical Engineering Science* 77, 130-142.
- Schwarzenbach, D., 1997. *Crystallography*, first ed. Wiley.
- Wan, J., Ma, C.Y., Wang, X.Z., 2008. A method for analyzing on-line video images of crystallization at high-solid concentrations. *Particuology* 6, 9-15.
- Wan, J., Wang, X.Z., Ma, C.Y., 2009. Particle shape manipulation and optimization in cooling crystallization involving multiple crystal morphological forms. *AIChE Journal* 55, 2049-2061.
- Wang, X.Z., Calderon De Anda, J., Roberts, K.J., 2007. Real-Time Measurement of the Growth Rates of Individual Crystal Facets Using Imaging and Image Analysis: A Feasibility Study on Needle-shaped Crystals of L-Glutamic Acid. *Chemical Engineering Research and Design* 85, 921-927.
- Wang, X.Z., Roberts, K.J., Ma, C.Y., 2008. Crystal growth measurement using 2D and 3D imaging and the perspectives for shape control. *Chemical Engineering Science* 63, 1173-1184.
- Wold, S., Sjöström, M., Eriksson, L., 2001. PLS-regression: a basic tool of chemometrics. *Chemometrics and Intelligent Laboratory Systems* 58, 109-130.
- Zahn, C.T., Roskies, R.Z., 1972. Fourier Descriptors for Plane Closed Curves. *Computers, IEEE Transactions on* C-21, 269-281.
- Zhang, D., Lu, G., 2004. Review of shape representation and description techniques. *Pattern Recognition* 37, 1-19.
- Zhang, R., Ma, C.Y., Liu, J.J., Wang, X.Z., 2015. On-line measurement of the real size and shape of crystals in stirred tank crystalliser using non-invasive stereo vision imaging. *Chemical Engineering Science* 137, 9-21.
- Zhang, Y., Liu, J.J., Zhang, L., De Anda, J.C., Wang, X.Z., 2016. Particle shape characterisation and classification using automated microscopy and shape descriptors in batch manufacture of particulate solids. *Particuology* 24, 61-68.
- Zhang, Y., Sizemore, J.P., Doherty, M.F., 2006. Shape evolution of 3-dimensional faceted crystals. *AIChE Journal* 52, 1906-1915.
- Zhao, J., Wang, M., Dong, B., Feng, Q., Xu, C., 2013. Monitoring the Polymorphic Transformation of Imidacloprid Using in Situ FBRM and PVM. *Organic Process Research & Development* 17, 375-381.

Zhou, Y., Lakshminarayanan, S., Srinivasan, R., 2011. Optimization of image processing parameters for large sets of in-process video microscopy images acquired from batch crystallization processes: Integration of uniform design and simplex search. *Chemometrics and Intelligent Laboratory Systems* 107, 290-302.

Zhou, Y., Srinivasan, R., Lakshminarayanan, S., 2009. Critical evaluation of image processing approaches for real-time crystal size measurements. *Computers & Chemical Engineering* 33, 1022-1035.

Ziegler, G.M., 1995. *Lectures on polytopes*, first ed. Springer, New York.

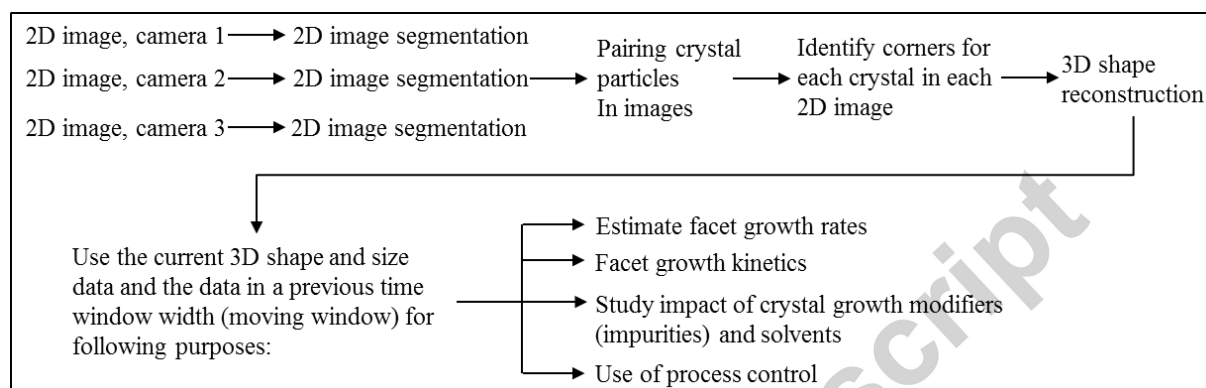


Fig.1. The steps involved in stereo imaging of crystallisation processes based on a triangulation algorithm for 3D crystal shape reconstruction

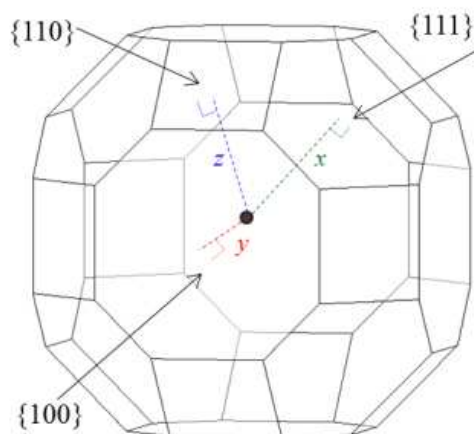


Fig.2. The morphology of a potash alum crystal and the three characteristic sizes (x, y, z) for the three independent faces.

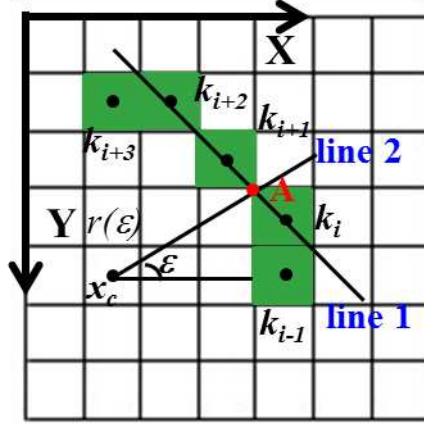


Fig. 3. An example of signature in the pixel coordinate system. X and Y represent the axes in the pixel coordinate system, and x_c is the centre of a particle's projection. The distance $r(\epsilon)$ and the angle ϵ are the polar coordinates of point A on the boundary. Lines 1 and 2 are the linearly connecting lines of neighbouring pixel points and the ray from the centre respectively. $k_{i-1}, k_i, k_{i+1}, k_{i+2}, k_{i+3}$ are the pixel points on the boundary of the particle's projection.

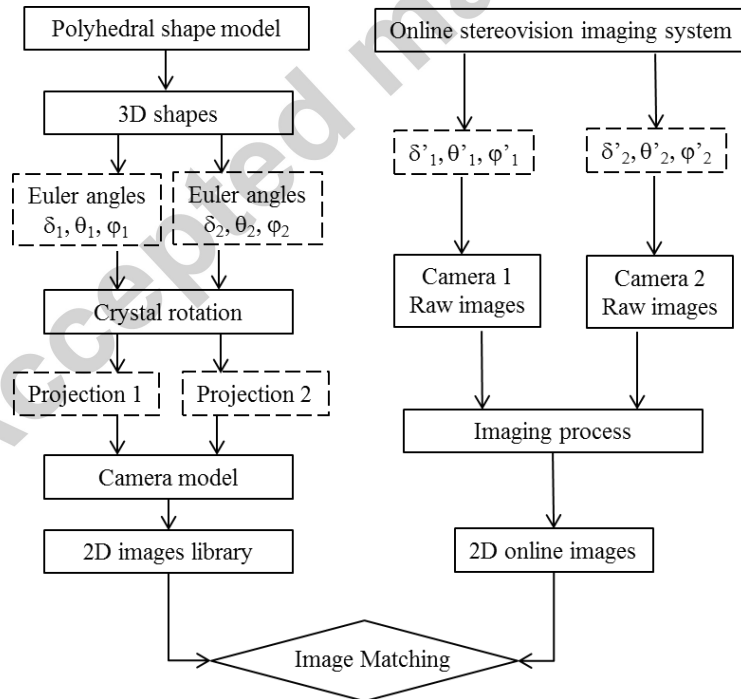


Fig.4. The framework for the integration of polyhedral shape model and online stereovision imaging system

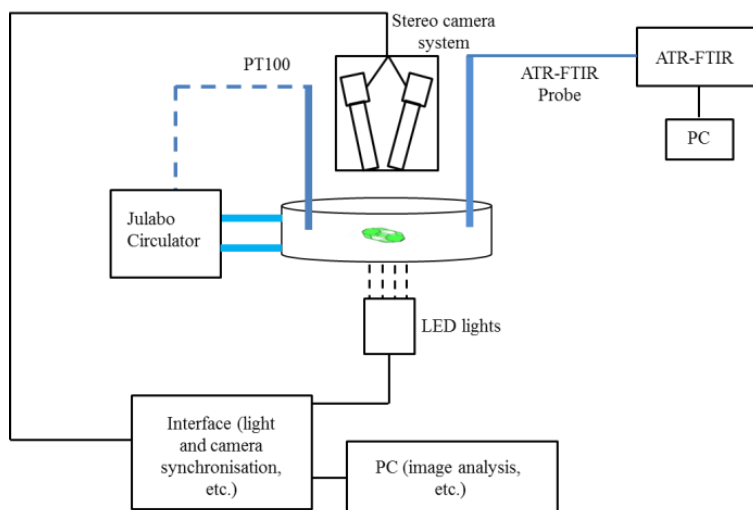
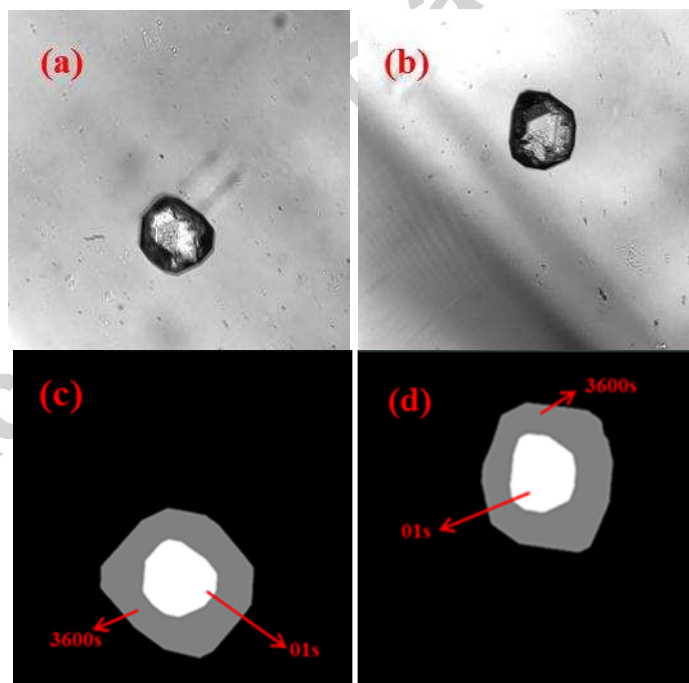


Fig.5. Schematic of the experimental set-up equipped with the stereovision imaging system.



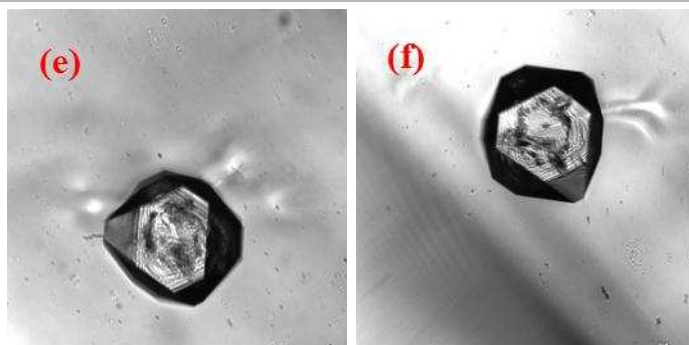


Fig.6. (a) and (b) are real images taken by camera 1 and camera 2 at time 1s, and the white areas of (c) and (d) are their image segmentation results. (e) and (f) are real images taken by cameras 1 and 2 at time 3600s, and the gray areas in (e) and (f) are their image segmentation results.

Accepted manuscript

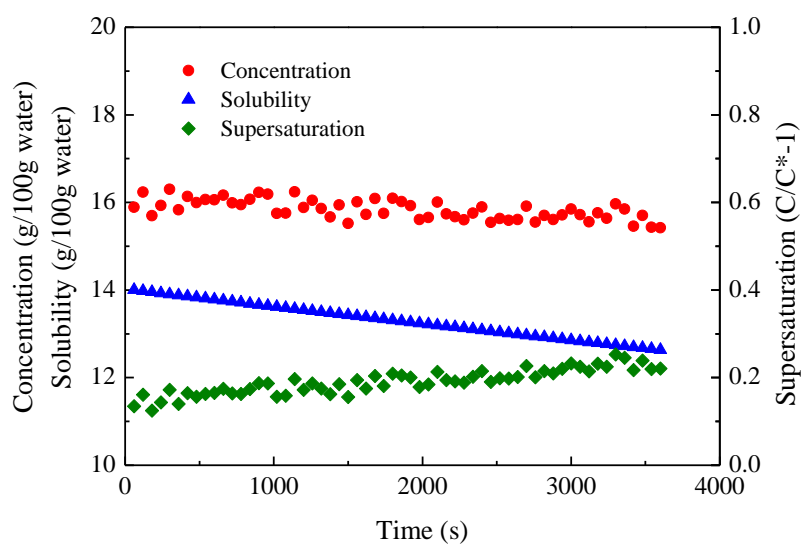


Fig.7. Evolution of solution concentration (●), solubility (▲) and the relative supersaturation (◆) with time.

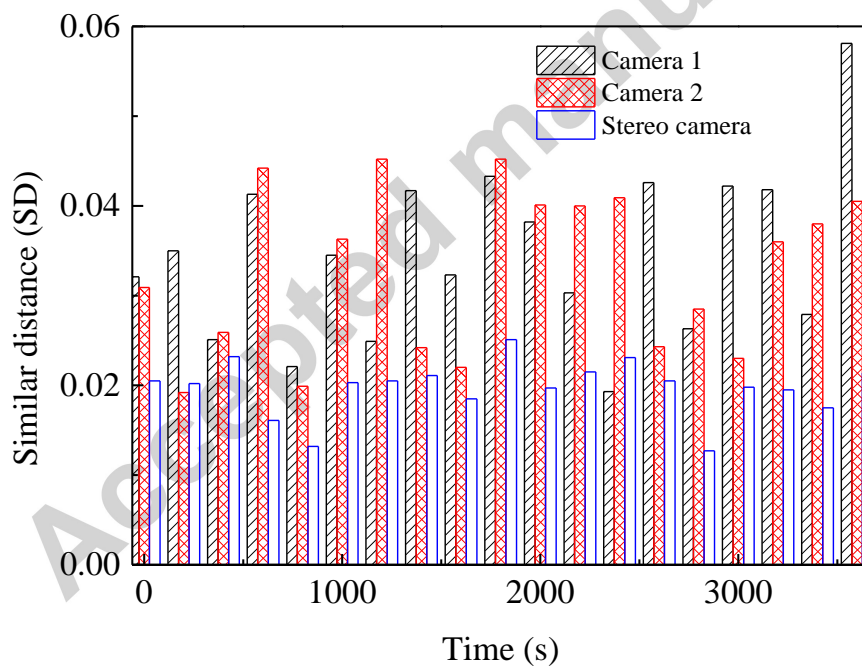


Fig.8. The comparison of SD using single camera and stereo camera

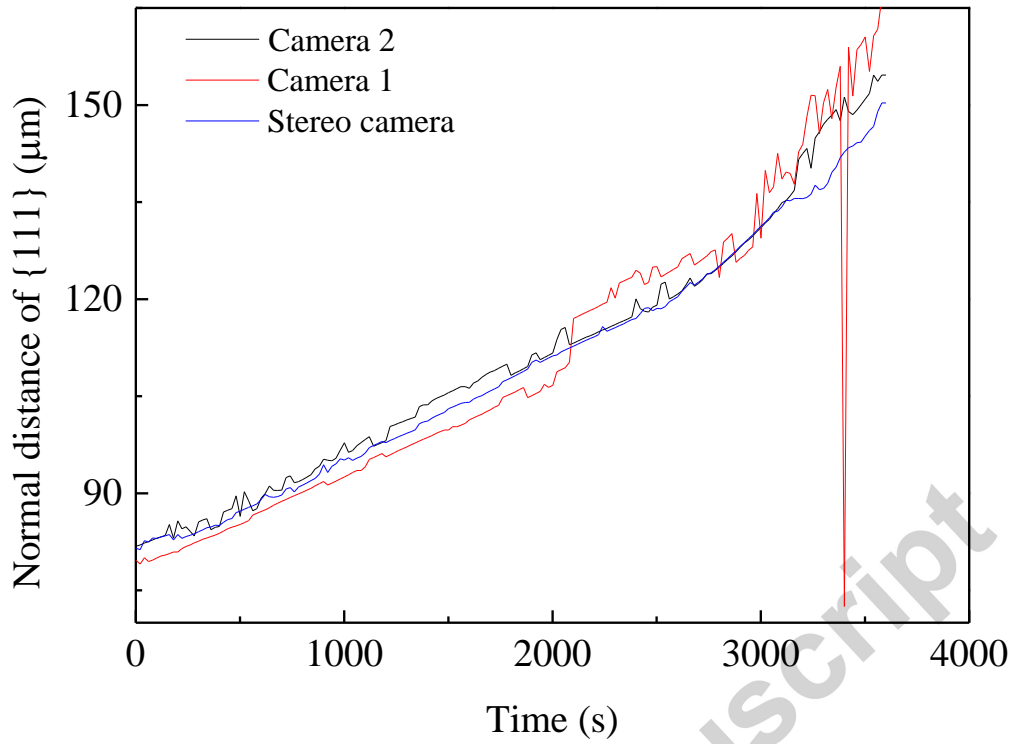
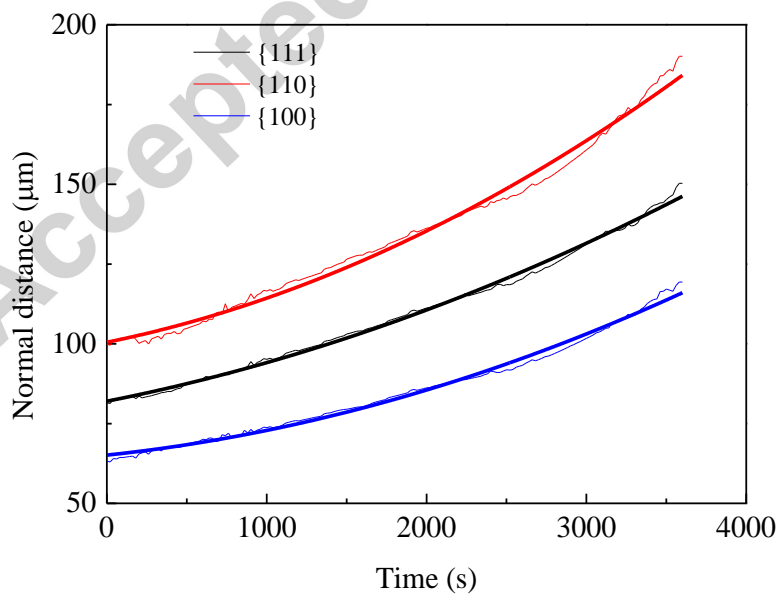
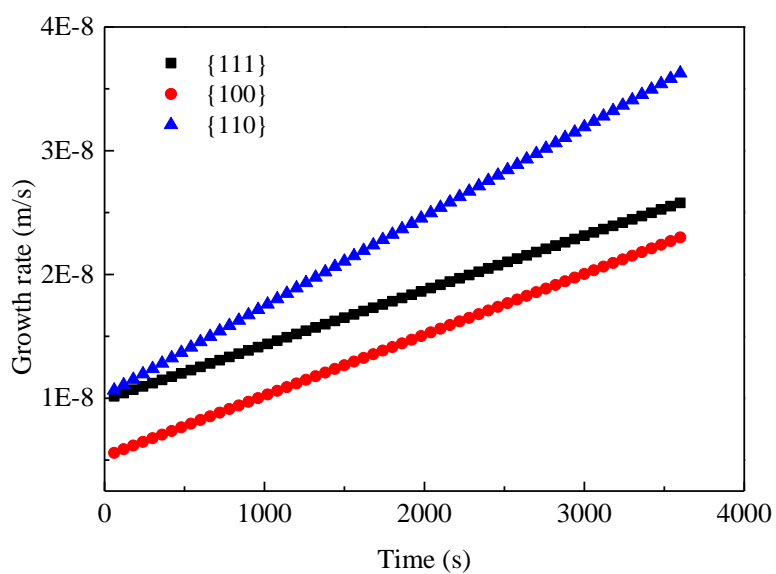


Fig.9. The comparison of the estimated normal distance of {111} using single camera and stereo camera.



(a)



(b)

Fig.10. The normal distances (a) and the corresponding growth rates (b) of three individual faces, estimated by stereo imaging technique

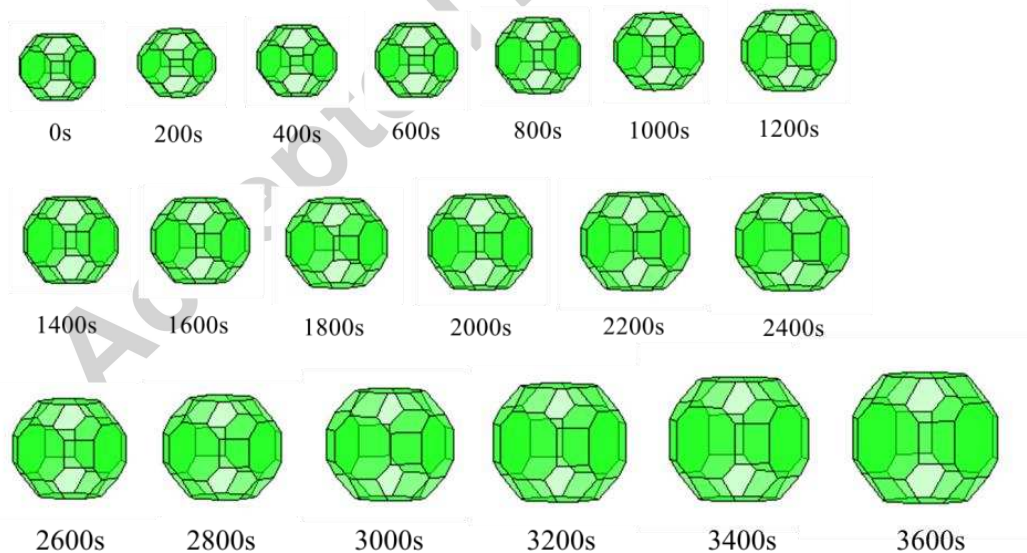


Fig.11. Crystal shape evolution of potash alum

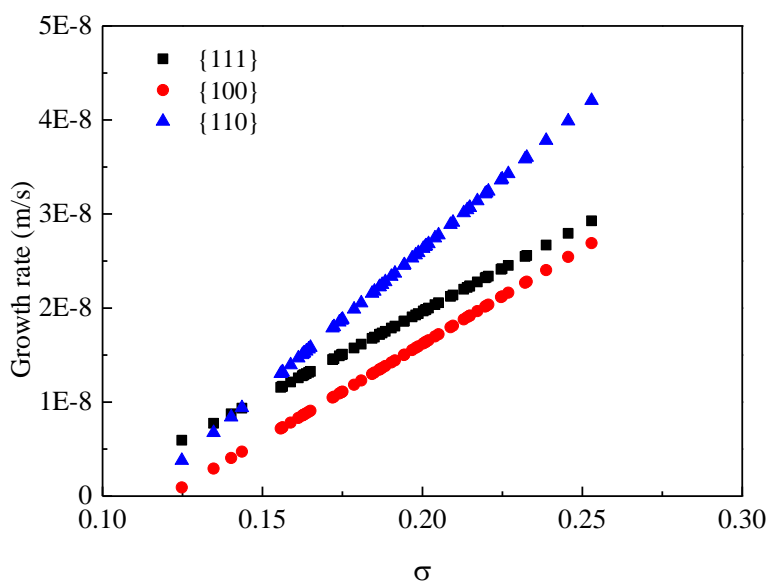


Fig.12. Crystal growth rates of three individual faces plotted against the relative supersaturation (solid triangles- $\{110\}$ face; solid circles- $\{100\}$ face; solid squares- $\{111\}$ face).
















Table 1 Experimental matrix for ATR FTIR calibration data collection at different potash alum concentration and temperatures*

Concentration (g/100g water)\temp($^{\circ}$ C)	10	20	30	40	50
2					
4	s				
6		s		s	
8			s		
10		s		s	s
12			s		
14				s	
16					s
18				s	
20					
24					s
Solubility (g/100g water)	7.5	11.41	16.4	23.48	36.02

* cells marked with label 's' were the spectra used for model validation; the rest for model training

Table 2 Application to potash alum crystallisation*

Time (s)	Real images		Processed images		Single Camera	StereoCamera		3D reconstructed morphology of crystal
	C1	C2	C1	C2	SD ($\times 10^{-2}$)	Estimated size (x, y, z (μ m))	SD ($\times 10^{-2}$)	

0					C1: 3.21 C2: 3.09	C1 (79.63, 64.70, 97.88) C2 (81.81, 60.33, 101.2)	2.05	(81.52, 63.17, 99.86)	
1800					C1: 4.03 C2: 3.89	C1 (105.4, 84.61, 129.3) C2 (108.2, 82.53, 133.9)	2.97	(107.8, 83.58, 132.1)	
3200					C1: 3.38 C2: 2.95	C1 (143.9, 126.6, 166.3) C2 (142.5, 105.9, 175.3)	2.14	(135.5, 107.6, 171.4)	

* C1, C2 – camera 1, camera 2; SD – similarity distance, calculated by equation (20)

Highlights

- A stereo imaging camera model is proposed for reconstruction of 3D crystals shape.
- The new method is more robust than the previous triangulation algorithm, in particular for complex crystal shape
- On-line 3D crystal shape imaging is also used to derive crystal faced growth kinetics